Acta Materialia 144 (2018) 459–469

Contents lists available at ScienceDirect

Acta Materialia

journal homepage: www.elsevier.com/locate/actamat

Full length article

Wetting and solidification of silver alloys in the presence of tungsten carbide

Nachiketa Ray*, Ludo Froyen, Kim Vanmeensel, Jef Vleugels

KU Leuven, Department of Materials Engineering, Kasteelpark Arenberg, 44, B-3001 Heverlee, Belgium

ARTICLE INFO

Article history:
Received 21 October 2017
Accepted 5 November 2017
Available online 9 November 2017

Keywords:
Metal matrix composites
Powder metallurgy
Contact angle
Solidification
Electron backscattered diffraction

ABSTRACT

The wettability of pure Ag and Ag alloys (with Ni and Cu) on WC was investigated as a function of temperature by means of sessile drop experiments. Ni was found to preferentially segregate at the Ag/WC interface resulting in a decreased contact angle as compared to Cu. The influence of the Ni content and WC particle size on the solidification behavior of Ag in infiltrated Ag-WC-Ni (40 wt% WC and 0.07/5 wt% Ni) composites was assessed, revealing the pushing of WC particles by the solidification front, especially in the materials with a finer WC particle size. Addition of Ni decreased the grain size of the Ag phase by promoting heterogeneous nucleation. Complete coherency between the Ag and Ni phases was confirmed by electron backscattered diffraction analysis.

1. Introduction

The use of a metallic binder in brittle ceramics has been of considerable interest in order to find a balance between toughness and hardness. Refractory metal carbide rich composites, commonly known as cemented carbides, are popular in the cutting tool industry whereas conductive metal rich composites are used as electrical contact materials. Silver based refractory metal/metal carbides are known for their excellent resistance to electric arcs and are established to operate at medium (10–100 A) or high currents (1–100 kA) [1,2]. Although the electrical and thermal properties of these materials are of major relevance for the electrical industry [3], the science behind the processing of these materials appeals to a broader readership. The manufacturing process involves combining two or more compounds which have negligible solubility in both the solid and liquid phase [4]. Although it is a desired feature for the application, as the individual properties of each phase are retained, the fabrication of these materials presents serious challenges.

Ag-WC/W composites consisting of WC/W particles in a Ag matrix are mainly prepared by powder metallurgical routes which involves powder compaction followed by densification. Although researchers have managed over time to densify these materials up to 99% of the theoretical density, a stable porosity-free production of these composites has been a challenge. The traditional densification step involves 'cold press-sinter-infiltration' at temperatures above the melting point of silver. Therefore, two physical aspects of the process have been investigated in this work. The first one is the wetting behavior of silver and tungsten carbide, which would determine the likelihood of the silver to adhere to the WC above its melting point. Sessile drop experiments have been regarded as one of the most popular methods to measure the contact angle, allowing to estimate the interfacial energy by solving the Young's equation. Although the contact angle of silver at its melting point on tungsten [5,6] and tungsten carbide [7] substrates has been measured before, it has been pointed out that the contact angle strongly depends on factors like, temperature [6,8], substrate roughness [9–11], drop size [10] and oxidation of substrate [11]. In this work, a *wettable flat* substrate as defined by Nakae et al. to have a surface roughness in-between 0.01-0.5 μm [9] and a low oxygen content have been used. The effect of temperature and alloying elements like Ni and Cu were investigated. The second part of this work is focused on the solidification behavior of silver in the vicinity of WC. Solidification of metal-matrix particulate composites has been extensively studied in terms of the chemistry and mechanics of wetting, the influence of particles on nucleation, the growth of the solid metal with stationary/mobile reinforcements and chemical reactions at the liquid/solid interfaces [12,13]. Since Ag and WC show no evident chemical reaction or phase solubility, this study is mainly focused on the growth of the silver grains and their preferred orientation.

* Corresponding author.
E-mail address: nachiketa.ray.1014@gmail.com (N. Ray).

https://doi.org/10.1016/j.actamat.2017.11.012
1359-6454/

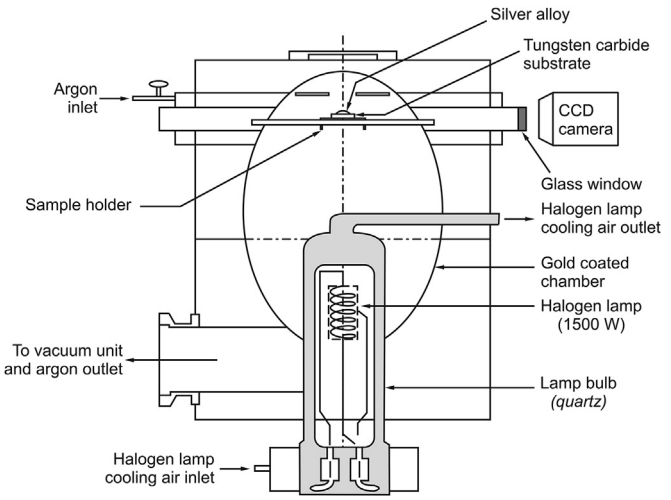

Fig. 1. Schematic showing the construction of the SVF17SP heating system used for contact angle measurements.

2. Experimental procedure

2.1. Contact angle measurement

A Ø 30 mm disc of WC was densified from WC powder (d_{50} = 0.8 μm) to 99.9% theoretical density by spark plasma sintering at 1900 °C and 65 MPa for 5 min. The dense block was machined into thin plates of 6 mm × 6 mm × 0.4 mm using electrical discharge machining and ground on all surfaces to generate plane-parallel surfaces. The top surface of the ground substrates was further polished using 3 μm and 1 μm diamond suspension (Kemet) on a polishing cloth (TOUCHLAM® 2TS3, LAM PLAN). The surface roughness of the substrates was measured using a profilometer (Surtronic 3+, Taylor-Hobson), having a resolution of 0.01 μm. Five measurements on five identical WC substrates were measured over a length of 1.25 mm.

Pure silver and $AgNi_{0.15}$, $AgCu_{0.2}$, $AgCu_1$ and $AgCu_{0\cdot2}Ni_{0.15}$ (all values in wt.%) alloys, as extruded in wire form, were used in this investigation. Identical volumes (2 mm^3) of each alloy were carefully placed on top of the WC substrate. This configuration was placed on an alumina hot stage connected to a B-type thermocouple. The SVF17SP heating system was an attachment of a Confocal Scanning Laser Microscope (1LM21-SVF17SP, Lasertec), which was not used in this work. The heating system is basically a small furnace which consists of a 1500 W halogen lamp ideally placed at one of the foci of a reflective ellipsoidal chamber (gold plated), which reflects the light to the other focal point of the ellipsoid, where the sample was strategically positioned. The thermocouple is connected to a PID controller which enables to achieve precise and rapid heating and cooling rates. A glass window (10 SCS 1 DIN, SVAR welding glass, Severosklo) is foreseen at the same height of the sample holder which allows to capture images of the side view of the sample by means of a CCD camera. A detailed schematic of the furnace is shown in Fig. 1. The furnace temperature was calibrated using pure silver and pure copper at their respective melting points and the difference between real and measured temperature was observed to be almost similar at 961.8 °C and 1085 °C with a variation of 0–5 °C. The heating profile consisted of a steep ramp of 200 °C/min up to 900 °C followed by a gradual increase (5 °C/min) in temperature up to 1150 °C, during which the molten metal and substrate configuration was captured by a CCD camera. The cooling cycle was not recorded in order to evade supercooling effects. The camera captured images at 1 frame/s having an image size of 225 kB/frame. Purified argon (argon gas flowing through a Mg powder bed at 500 °C) was used as ambient gas for all experiments at a flow rate of 10 l/hr. After the ellipsoidal chamber was sealed, it was evacuated using a turbomolecular pump, followed by flushing the chamber with purified Ar. This cycle was repeated 3 times in order to ensure minimum oxygen contamination.

The captured images were analyzed by image processing software (ImageJ) using a Java plugin (Drop analysis, LB-ADSA [14]) to measure the contact angle made by the silver alloy on the tungsten carbide substrate as a function of temperature. The interface between the silver alloy and tungsten carbide after the test was investigated using Electron probe micro-analysis (EPMA, JXA-8530F, JEOL).

2.2. Solidification studies

The melting and solidification temperatures of the five silver alloys were characterized using differential scanning calorimetry (DSC, Q600 SDT, TA Instruments). The alloys were first placed in an alumina pan and heated to 1000 °C and cooled down in order to melt and make a thorough contact with the crucible. Then the alloys were re-heated and cooled at 2 °C/min and 10 °C/min respectively for heat flow measurement as a function of temperature and time.

Pressureless molten metal infiltration of porous sintered pellets was carried out in order to investigate the solidification behavior of silver in the vicinity of WC particles. The porous sintered pellets (Ø 7 mm) were prepared by liquid phase sintering of uniaxially pressed Ag, WC and Ni powder mixture discs at 970 °C for 30 min. Three material types with varying WC particle size and Ni content were prepared for the current investigation as summarized in Table 1. The median particle size (d_{50}) of Ag and Ni was 5 μm and 7 μm respectively. The sintered pellets were infiltrated by silver on a graphite crucible at 1070 °C for 30 min (video, supplementary material) which allowed the composite to achieve near theoretical density (>99%) as measured using Archimedes' principle (Table 1). Both sintering and infiltration were carried out in a reducing H_2:N_2 (3:1) atmosphere in order to prevent oxidation of the tungsten carbide. Since the infiltrated pellets were only in contact with the graphite crucible (heat sink) at the bottom, it can be assumed that during cooling (furnace cooling), heat was mainly lost through the bottom of the infiltrated pellets thus resulting in directional solidification.

Supplementary video related to this article can be found at https://doi.org/10.1016/j.actamat.2017.11.012.

Table 1
Materials investigated in this work, tabulating WC particle size, starting powder composition, final composition after infiltration (balance WC) and relative theoretical density.

Material	WC d_{50} (μm)	Powder composition		Final composition		Density ($g\cdot cm^{-3}$)	Relative TD (%)
		Ag (wt.%)	Ni (wt.%)	Ag (wt.%)	Ni (wt.%)		
WC08Ni007	0.8	40	0.1	60	0.07	11.99	99.30%
WC40Ni007	4.0	40	0.1	60	0.07	12.03	99.64%
WC08Ni500	0.8	46	6.0	55	5	11.83	98.94%

2.3. Microstructural and texture characterization

The infiltrated samples were sectioned and appropriate metallographic preparations were carried out. A single step grinding process was carried out using a MD-Allegro™ (Struers) grinding disc for 10 min at 150 rpm with a 15 μm diamond suspension (Kemet) to provide a flat surface. Post grinding, the samples were polished with 3 μm and 1 μm diamond suspension (Kemet) on a TOUCHLAM® 2TS3 (LAM PLAN) polishing cloth. The final polishing was carried out with an OP-S (0.25 μm) colloidal silica suspension (Struers) on OP-Chem (Struers) polishing cloth. The polished samples were electrochemically etched with a mixture of 1% perchloric acid, 9% glycerol and 90% methanol (vol%) under 20 V DC supply for 20 s. During etching, the electrolyte was kept at −60 °C using liquid nitrogen. The etching of the silver phase was carried out to investigate the samples with a polarized light microscope (Axioskop 40 Pol/40 A Pol, Carl Zeiss). Since silver is very ductile, a small strain is always induced during any form of mechanical polishing, thus in order to minimize external strains, small regions of the samples were Ar ion milled using a cross section polisher (IB-09010CP, JEOL), in which a region of the sample is irradiated with a broad argon ion beam with an accelerating voltage of 6 kV. This method was only used to investigate the very low angle misorientation (2°–5°) within a grain, and is not ideal for studying large surfaces due to unreasonably long milling times.

Electron backscattered diffraction (EBSD) was carried out on all three sample types (Table 1) in a scanning electron microscope (Nova NanoSEM 450, FEI), using an accelerating voltage of 20 kV and spot size of 5 nm for all measurements. The scan step size and scan area was varied according to the requirement. Since silver and nickel have an identical crystal structure and similar lattice parameters, it is difficult for the OIM™ data collection software (EDAX) to correctly index them with a sufficient confidence index. In order to have an accurate dataset, a simultaneous energy dispersive spectroscopy (EDS) scan was also performed which was able to distinguish Ag from Ni. The orientation data generated from the Hough peaks recorded during the scan was recalculated using the EDS data in order to provide an accurate dataset with sufficiently high confidence index. The orientation data was analyzed using OIM™ analysis software. The data used for calculation and interpretation was always partitioned from the raw recorded data by defining constraints on confidence index and grain boundary misorientation. The selected data had a confidence index, (C.I.) > 0.1 and a grain was defined so that the boundary would have a misorientation ≥ 15° with its neighboring grain, and would at least have more than a single row of pixels and at least five pixels per grain. The pole figures obtained from EBSD data were calculated by discrete binning with a resolution of 5° and without enforcing any sample symmetry.

3. Results and discussion

3.1. Surface roughness

Arithmetical mean deviation (R_a) and the maximum height of the roughness profile (R_z) were calculated from the measured surface roughness profiles for all 25 polished WC substrates. The probability mass function of these two parameters were calculated and is plotted in Fig. 2. It should be noted that the roughness of the samples were very close to the resolution of the measuring device (10 nm), thus the calculated average absolute roughness is always below the resolution limit. However, the probability distribution shows that the maximum height roughness is not more than 20 nm. This enables us to declare the polished WC surfaces as *wettable flat* substrates, as defined by Nakae et al. [9].

3.2. Contact angle

The contact angle of the investigated silver alloys on the polished WC substrates was analyzed using low-bond axisymmetric drop shape analysis (LBADSA), which provides a first-order approximation of the Young-Laplace equation. The Young's relation (Eq. (1)) constitutes a force-balance between the interfacial energies between the solid, liquid and vapor interfaces on a simplified planar geometry, where θ is defined as the contact angle between the liquid-gas interface and the solid-liquid interface through the liquid. γ represents the interfacial energy between solid-gas (γ_{SG}), solid-liquid (γ_{SL}) and liquid-gas (γ_{LG}) interface.

$$\gamma_{SG} = \gamma_{SL} + \gamma_{LG} \cdot \cos\theta \quad (1)$$

The measured contact angles (θ) after the onset of melting of the respective alloys has been plotted in Fig. 3 as a function of

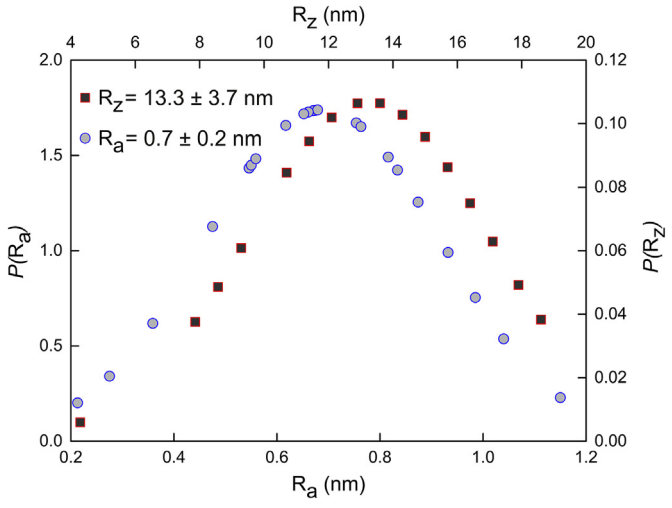

Fig. 2. Discrete probability distribution showing the probability mass function, $P(x)$ for the arithmetical mean deviation (R_a) and the maximum height of the roughness profile (R_z) of the polished WC substrates.

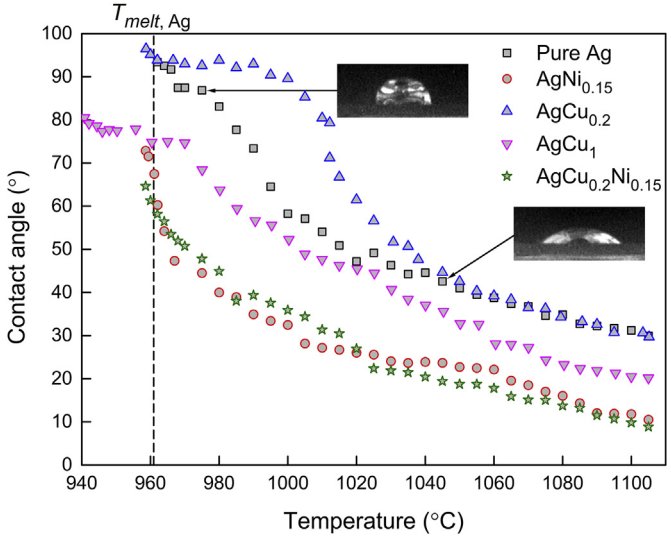

Fig. 3. Contact angles measured by low-bond axisymmetric drop shape analysis (LBADSA) as a function of temperature for different silver alloys (values in wt.%) on a pure WC substrate. The substrate-drop configuration was heated at 5 °C/min in purified argon.

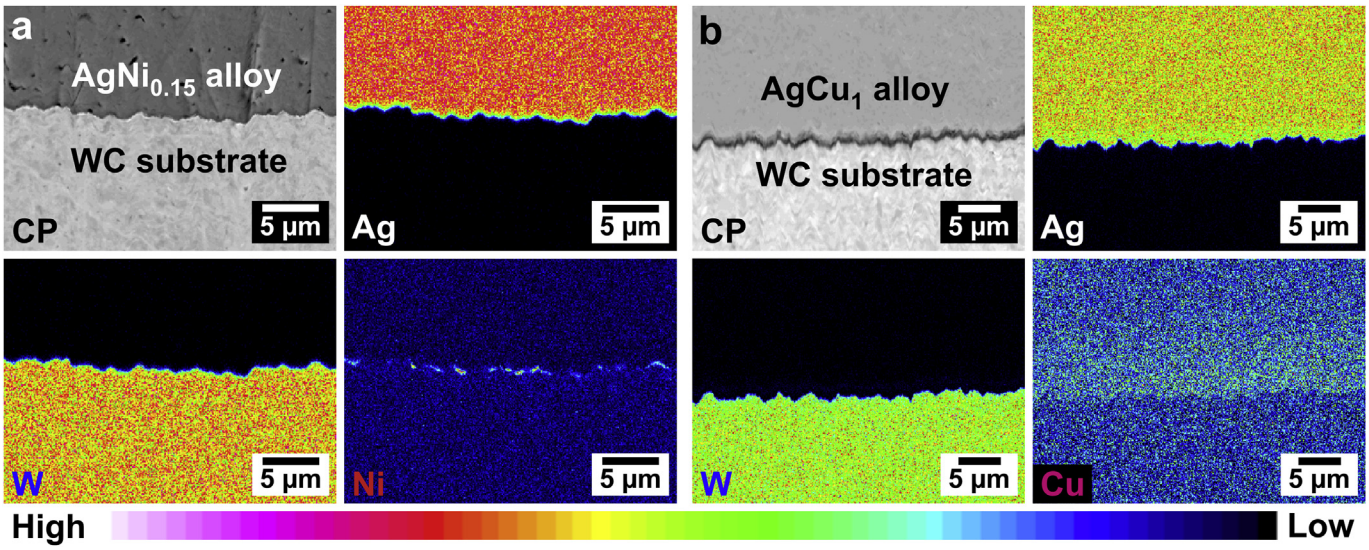

Fig. 4. Wavelength dispersive spectroscopy elemental mapping of the interface between the WC substrate and (a) $AgNi_{0.15}$ and (b) $AgCu_1$ alloy after heating to 1150 °C.

temperature. Representative images captured by the CCD camera for the pure silver droplet are shown in the inset corresponding to its temperature. The contact angle of pure silver on WC and WC-Co alloys has been studied by Yamaguchi et al. who showed that the contact angle of silver on WC decreased from 150° to 140° while heating at 10 °C/min in argon [7]. Factors like surface roughness of the substrate and oxygen content were however not specified, which is the reason behind the large discrepancy of the reported results.

It is clear from Fig. 3 that the wetting of silver and the respective alloys improves with increasing temperature. Addition of Ni has a superior influence compared to the addition of Cu as the $AgNi_{0.15}$ alloy shows a better wetting behavior than $AgCu_{0.2}$ or $AgCu_1$ alloy. In contrast to the other alloys, $AgCu_{0.2}$ and $AgCu_1$ showed a steep decrease in wetting angle after a threshold temperature around 1010 °C for $AgCu_{0.2}$ and close to 970 °C for $AgCu_1$. Although Cu did not play a major role in improving the wettability, it did not diminish the effect of Ni as observed for the $AgCu_{0.2}Ni_{0.15}$ alloy, which showed the best wetting behavior at high temperatures.

It must be stated that, although the gaseous atmosphere (purified argon) during the experiments did not allow any further oxidation of the WC substrate, it had no contribution to reduce the native oxide film on the WC substrate. The presence of the native oxide film can be associated with the sudden drop in contact angle for some of the experiments in Fig. 3. Protsenko et al. [15] have shown the effect of surface chemistry of the W substrate on the contact angle, which changes as a function of temperature. For surfaces with an oxide film, the contact angle (θ) is an weighted average of θ_m and θ_{ox}, i.e. the contact angle of the liquid on the metal and oxide respectively based on the fraction of the surface covered by the oxide (α). This relation was provided by Cassie [16] as:

$$\cos\theta = \alpha\cos\theta_{ox} + (1-\alpha)\cos\theta_m \quad (2)$$

Therefore, it can be stated that with increasing temperature the surface chemistry of the WC substrate changed from a oxidized (WO_x) to a cleaner non-oxidized surface, resulting in both a gradual and sometimes sudden drop in contact angle.

In order to further investigate the effect of Ni and Cu and their influence on the wettability of Ag on WC, the substrate-droplet configuration after the sessile drop test was sectioned in order to analyze the interface between Ag and WC. Elemental mapping of the $AgNi_{0.15}$/WC and $AgCu_1$/WC interface was performed by wavelength dispersive spectroscopy (WDS) in an electron probe micro-analyser (EPMA, JXA-8530F, JEOL), as presented in Fig. 4. The color scale represents the qualitative concentration of the individual elements. The composition map (CP) shows the atomic number contrast of all the elements in one image, similar to a backscattered electron image. The $AgNi_{0.15}$/WC interface revealed a preferential segregation of Ni between Ag and WC as shown in Fig. 4 (a). However, no such segregation of Cu was observed at the interface (Fig. 4 (b)). This provides evidence that Ni preferentially precipitates at the Ag/WC interface during cooling. Macedo et al. showed that the late transition elements like Co, Ni and Fe easily spread on a WC surface, while Cu did not wet WC [17].

Since the surface tension of Ni is much higher than that of Ag ($\gamma_{LG,\,Ni} \approx 2\gamma_{LG,\,Ag}$) [6, p. 149–150], small additions of Ni would not influence $\gamma_{LG,\,Ag}$ [6, p. 155–161 and p. 243]. Therefore according to Young's equation (Eq. (1)), a decrease in contact angle of Ag by nearly 20° with the addition of 0.15 wt% of Ni is accounted by a decrease of the solid-liquid interfacial energy ($\gamma_{SL,\,Ag/WC}$), which is due to the adsorption of Ni at the interface.

3.3. Silver alloy solidification

The melting and solidification of the investigated silver alloys were studied using differential scanning calorimetry (DSC). The heat flow in and out of the alloys is displayed in Fig. 5 for a slow and fast heating and cooling rate. The amount of undercooling observed in all cases can be identified as the temperature difference between the onset of melting and solidification. It is clear that the amount of undercooling increases with increasing heating and cooling rate.

The addition of Cu decreased the onset of melting of the alloy [18] and also increased the amount of undercooling during solidification. During the processing of these materials at high temperatures (>800 °C), some gases evolved due to the slight oxidation of WC. These gases consist of volatile oxides and oxy-hydrates [$WO_2(OH)_2$] of tungsten [19] and water vapor. The water vapor is formed as a byproduct of the reduction of these oxides by hydrogen, which is present in all high temperature processing steps. Thus after the silver is solidified, the evolving gases, unless completely removed, would be entrapped as porosity in the

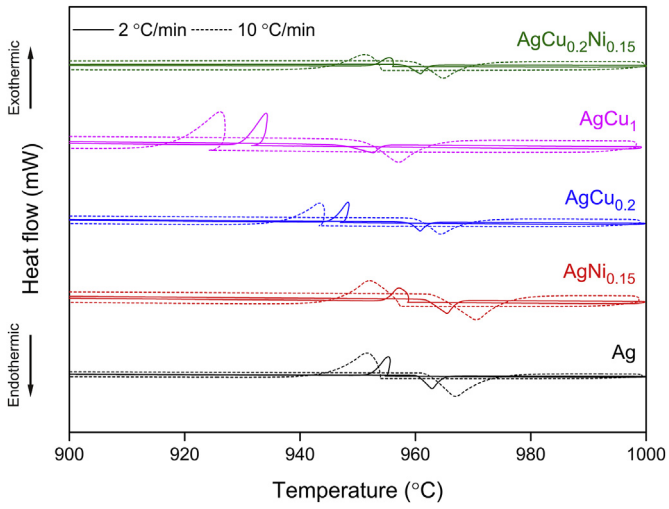

Fig. 5. Differential scanning calorimetry (DSC) curves of the silver alloys used in this study. Alloy compositions in wt.%.

solidified microstructure. This is one of the reasons why researchers have preferred a low 'melting' point alloy for infiltration [20]. However, the necessity is to have a low solidification temperature alloy which makes Cu a suitable alloying candidate, even though it did not provide a promising edge on the wettability.

3.4. Microstructure and crystallographic texture after solidification

Suitable metallographic preparation of the infiltrated composites were carried out for light and electron microscopy investigation. Fig. 6 shows the microstructure of the etched Ag-WC-Ni composite under polarized light. Large grains (~few mm) observed in WC08Ni007 (0.07 wt% Ni) correspond to silver oligocrystals formed after solidification. With increase in the amount of Ni, WC08Ni500 (5 wt% Ni), the grain size of the silver phase decreases due to the heterogeneous nucleation promoted by non-molten Ni phase.

Electron backscattered diffraction (EBSD) was used as a suitable technique to further characterize the microstructure and crystallographic texture of these composites. Formation of large grains (~1 mm) of cobalt and nickel binder phase has been reported in WC-based cemented carbides prepared by pressureless infiltration [21] and liquid phase sintering [22,23]. The binder phase has an identical crystallographic orientation over a large area independent of the texture of WC. However, no conclusive argument was provided to explain the above phenomenon. In this work, three materials have been studied (Table 1) with a variation in WC particle size and Ni content.

3.4.1. Ag-WC-Ni (0.07 wt%) material

The inverse pole figure (IPF) maps of the Ag and WC phases present in WC08Ni007, with 0.07 wt% Ni and WC particle size of 0.8 μm are shown in Fig. 7 (a) and (b). The color represents the orientation of the grains with respect to the direction perpendicular to the plane of the paper, i.e., the direction of powder pressing, infiltration and growth direction. Fig. 7 (c) shows the phase map distinguishing Ag and WC. The step size chosen for this measurement was 0.2 μm and the scanned area was 250 × 500 μm. Fig. 7 shows a representative cropped area (250 × 250 μm) of the measured scan in order to clearly visualize the WC grains at a higher magnification. Comparing Figs. 6 (a) and Fig. 7 (a), clarifies that the scanned area in EBSD is from one of the etched grains. Therefore the Ag phase displays a strong and sharp texture as shown in the (111) pole figure (Fig. 7 (d)). The WC grains are homogeneously dispersed in the silver matrix and do not seem to influence the orientation of Ag. A similar impression is derived from the IPF maps of WC40Ni007 (Fig. 8 (a) and (b)), i.e., the material containing a coarser grade of WC (4 μm) with the same amount of Ni. This measurement was also carried out with a step size of 0.2 μm and an area of 500 × 1000 μm was scanned. In the IPF map of the Ag phase, more than one grain is visible due to the very large scanned area. Therefore, it can be concluded that the WC particle size did not influence the grain size of the silver matrix. It was not possible from the IPF map to determine whether the WC grains assumed a preferred orientation. It should be noted that although in both the scans, the orientation of the Ag phase was

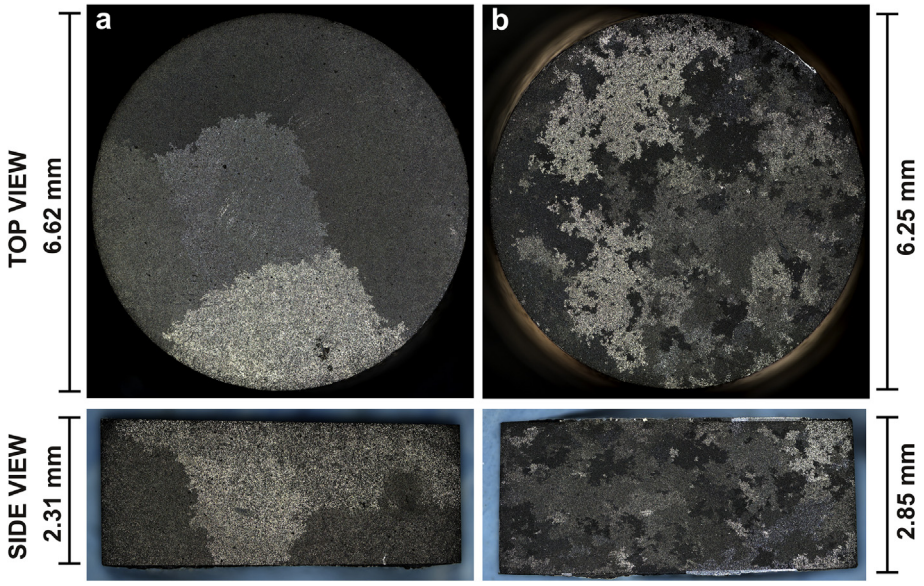

Fig. 6. Electrochemically etched surfaces of Ag-WC-Ni infiltrated composites observed under a polarized light microscope showing the top and side view of (a) WC08Ni007 and (b) WC08Ni500 (Table 1).

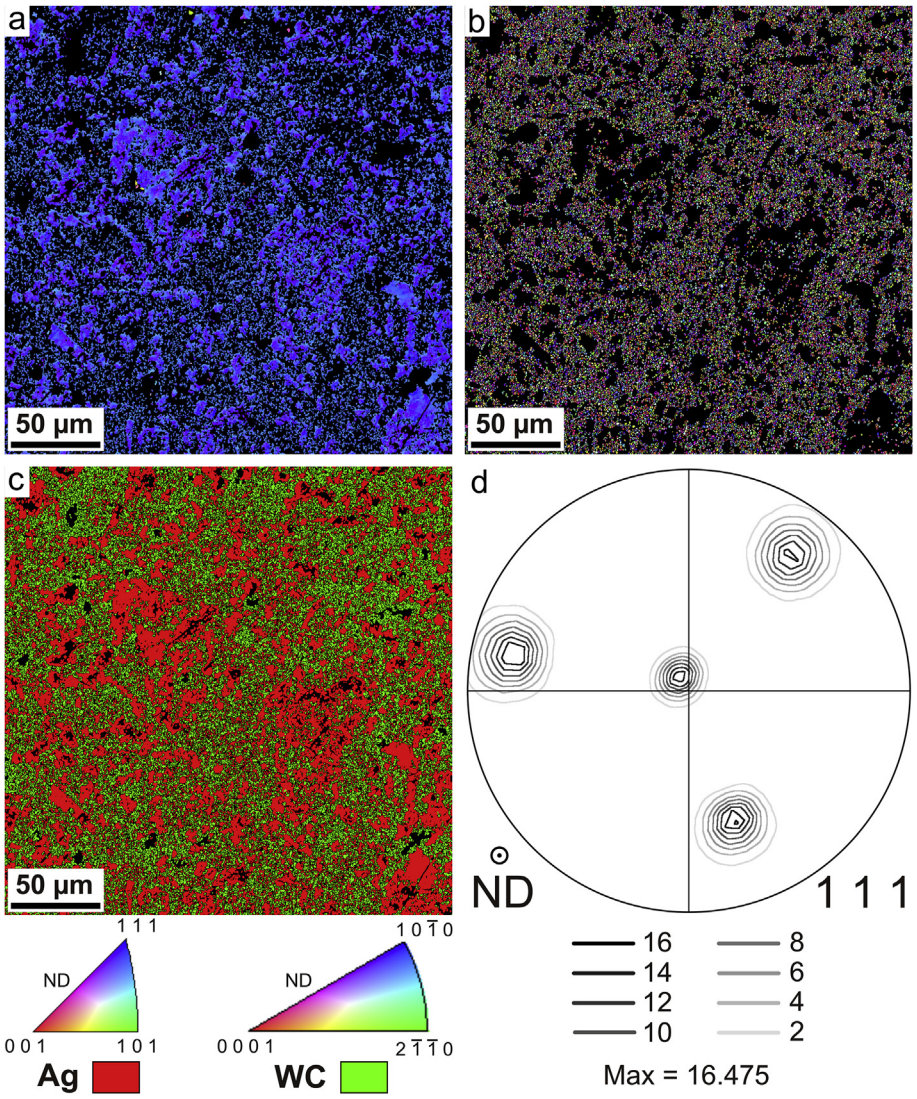

Fig. 7. Inverse pole figure maps showing the Ag (a) and WC (b) phases with grain boundaries having a misorientation ≥15° for WC08Ni007 (Table 1). (c) Phase map showing the distribution of the two phases. (d) (111) pole figure of the silver phase.

closely inclined towards the (111) plane normal, this was not the case for all silver grains. Other crystallographic orientations of Ag grains after infiltration have been reported in our previous work [[24], Fig. 7 (b)]. Both the scans shown in Figs. 7 and 8 were obtained after mechanical polishing to obtain an EBSD quality surface finish on a larger scale.

In order to minimize any external mechanical strain, a small area (100 × 100 μm) of WC08Ni007 was polished using a cross-section ion polisher and an area of (85 × 85 μm) was scanned for orientation imaging with a step size of 0.1 μm. The IPF maps of the Ag and WC phase are shown in Fig. 9 (a) and (b). The IPF of Ag shows that the grains are oriented in a crystal direction close to the (111) plane normal. These data were further partitioned into two datasets as shown in Fig. 9 (c) and (d) with respect to the crystal orientation. The silver present further away from the WC phase (Fig. 9 (c)) assumed a different crystal orientation than the silver present in the vicinity of the WC (Fig. 9 (d)). The difference in misorientation between these two partitions was between 3 and 5°, which can be defined as a very low angle grain boundary.

Growth of the solidified metal in the presence of mobile reinforcements (particle pushing) during processing of cast metal matrix composites is a well-known phenomenon [12,25–28]. During cooling, the solidification front can exert a force on the particles and push them along, thereby increasing the amount of particles in the last local solidifying liquid. The phenomenon of particle pushing however occurs below a certain critical velocity (V_c) of the advancing solidification front. Above this critical velocity, the particles would be captured by the moving front. Critical velocity depends on several factors like thermal conductivity, particle size and thermal gradient. Among the many theoretical models, let us select the ones which also considered heat flow around the particulate reinforcements. According to this model, if the thermal conductivity of the particle is higher than that of the surrounding liquid, a planar solidification front forms a depression under the particle, which is easily entrapped. However, if the thermal conductivity of the liquid is higher than for the particle, a bump is formed under the particle which gets pushed away [29,30]. Other researchers have modified the above criterion and have proposed to replace thermal conductivity by thermal diffusivity [31].

Since the thermal conductivity and thermal diffusivity of liquid silver [32] is higher than for WC [33] at any given temperature, it is

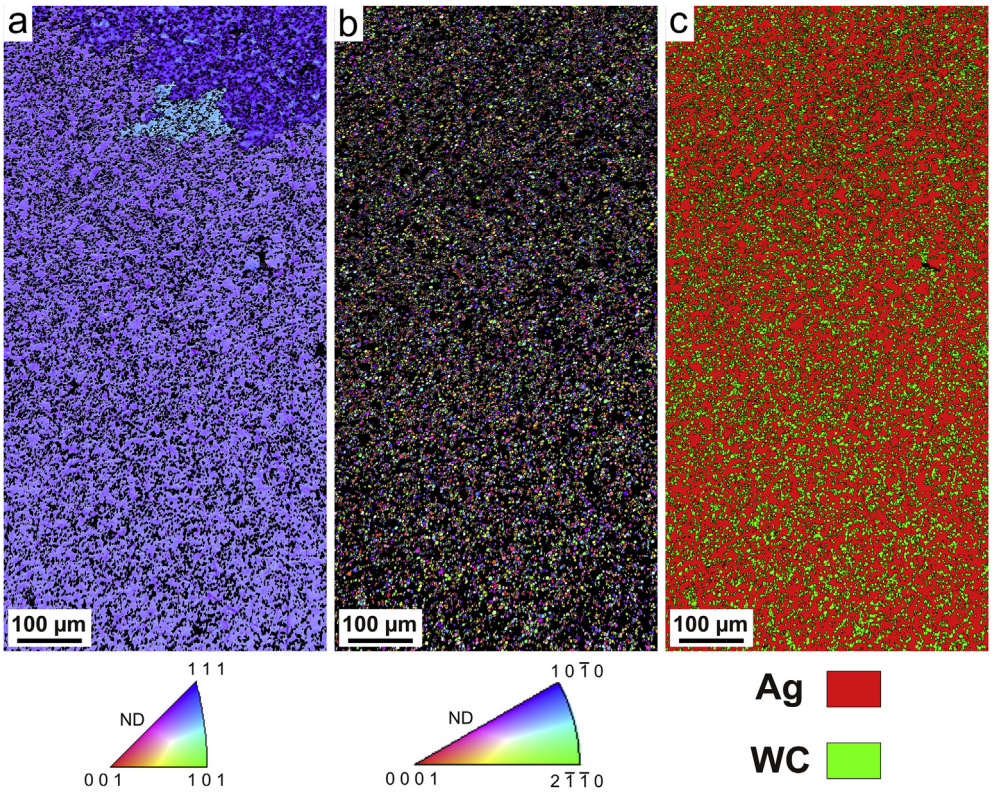

Fig. 8. Inverse pole figure maps showing the Ag (a) and WC (b) phases with grain boundaries having a misorientation ≥15° for WC40Ni007 (Table 1). (c) Phase map showing the distribution of the two phases.

reasonable to assume that isolated WC particles can be pushed away by the solidification front towards the WC rich sintered skeleton. During cooling, the Ag further away from the WC (Fig. 9 (c)) is solidified first, while the Ag present in the vicinity of the 'hotter' WC (Fig. 9 (d)) is still at a higher temperature. Thus the silver in the WC skeleton cools at a lower rate than the silver away from it. This is also evident from the IPF in which it is clear that the Ag in the WC skeleton assumes an orientation closer to a low index plane such as (111), with a lower interfacial energy. Thus it can be concluded that all isolated WC particles present in the

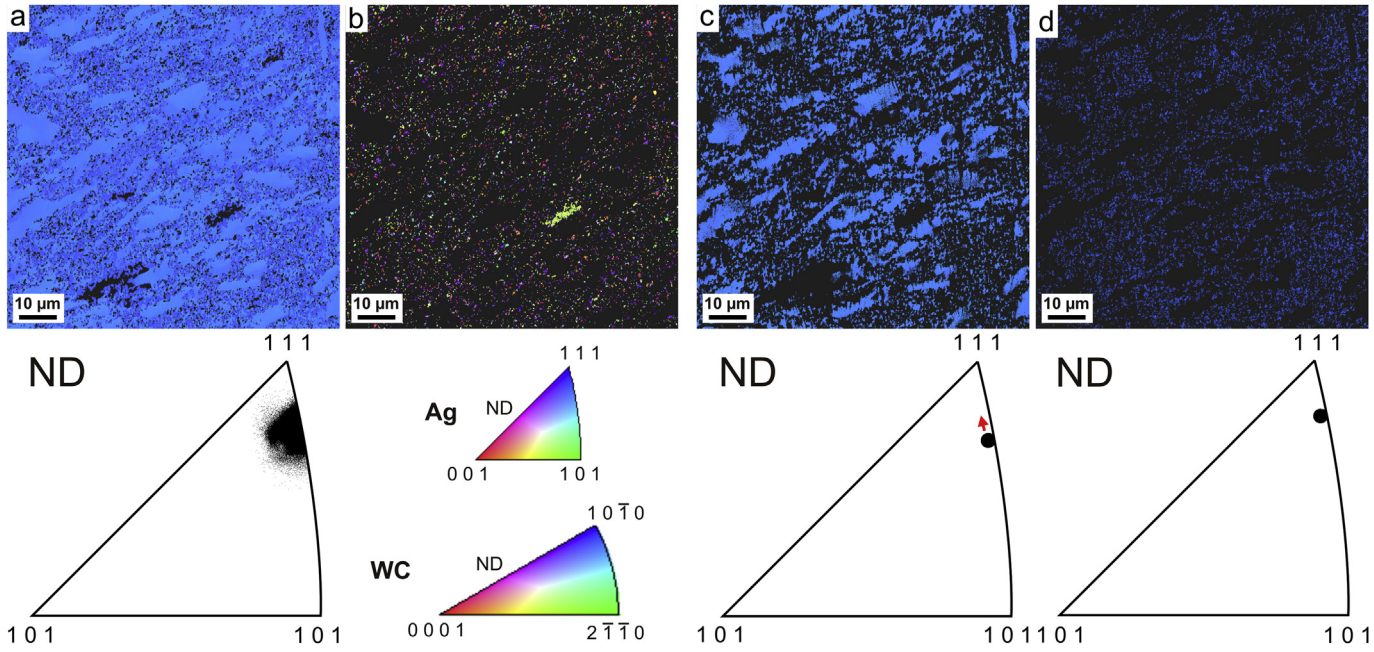

Fig. 9. Inverse pole figure maps showing the Ag (a) and WC (b) phases of WC08Ni007 (Table 1) polished by argon ion milling. Partitioned dataset of the silver phase further away from the WC (c) and in the vicinity of WC (d).

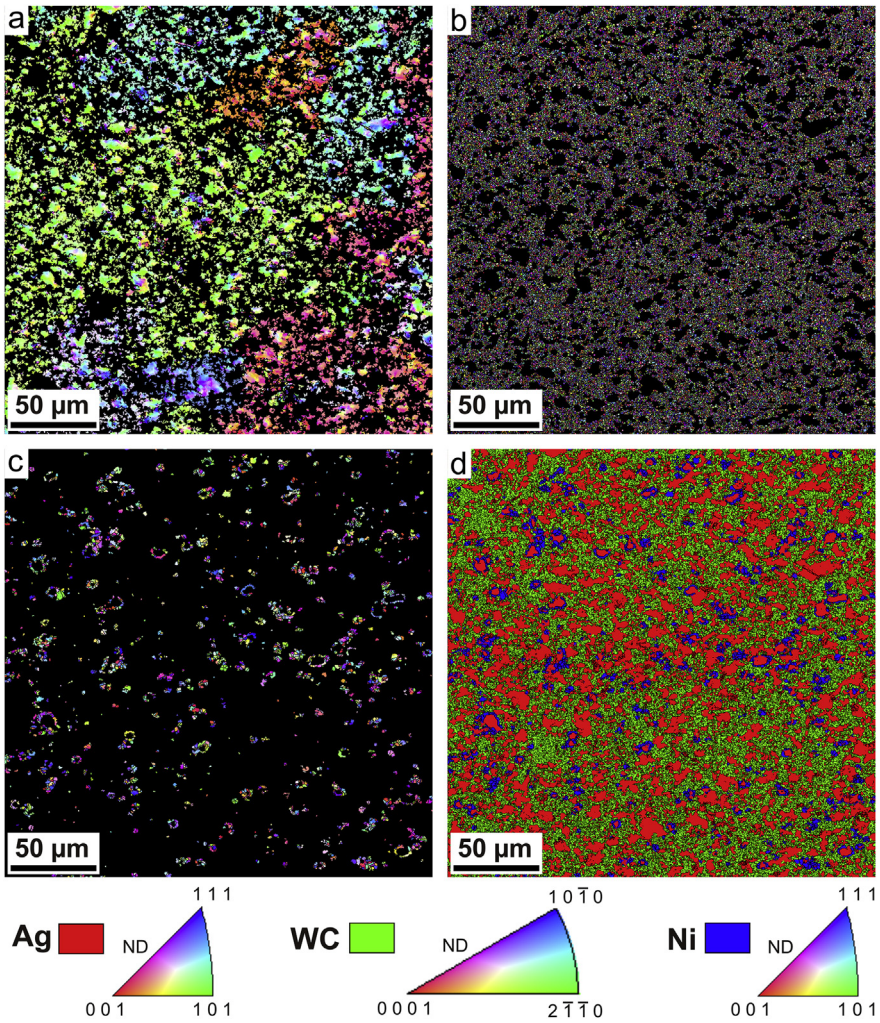

Fig. 10. Inverse pole figure maps showing the Ag (a), WC (b) and Ni (c) phases with grain boundaries having a misorientation ≥15° for WC08Ni500 (Table 1). (d) Phase map showing the distribution of the three phases.

silver rich area were pushed by the solidification front towards the WC rich areas, i.e., the region of the last solidifying liquid.

As mentioned before, the particle size of the reinforcement also influences the critical velocity (V_c) of the solidification front [25,34,35]. As the particle size increases, V_c decreases thus increasing the probability of particle engulfment rather than particle pushing. Thus it can be stated that less particle pushing is observed in WC40Ni007, i.e., the material containing coarser WC. Comparing Figs. 7 and 8, the silver rich areas are free from WC in the material processed from finer WC powder, thus showing more segregation of each phase compared to the coarser WC powder based material. However, other effects like sinterability is also strongly influenced by the particle size [3] and might have a major contribution towards the homogeneity. Yet the effect of particle pushing resulting in WC-free areas in the microstructure cannot be ignored.

3.4.2. Ag-WC-Ni (5 wt%) material

Figs. 5 and 6 clearly indicates that the addition of Ni promotes heterogeneous nucleation of the silver phase leading to a smaller Ag grain size. Therefore WC08Ni500, containing 5 wt% of Ni, was investigated by EBSD and the IPF and phase map is shown in Fig. 10. An area of 250 × 700 μm was scanned with a step size of 0.3 μm, however only a representative area of 250 × 250 μm is shown in Fig. 10. The IPF based microstructure shows that Ni surrounds the Ag phase, as also observed in our previous work [36]. At the maximum processing temperature of these materials in this work (1070 °C), Ni never reaches the liquid phase as verified from calculated phase diagrams [36]. However a small amount of Ni will dissolve in Ag in the liquid phase at elevated temperatures, which is precipitated again from the melt during solidification due to decrease in solubility.

In order to study the crystallographic orientation of Ag and Ni, the (111), (110) and (001) pole figures were calculated, as presented in Fig. 11. It is quite evident from both scans that Ag and Ni share an identical crystallographic orientation although the texture strength of Ag is higher than for the Ni phase. It is also interesting to observe a drop in texture strength of the silver phase with the addition of Ni, when comparing Figs. 7 (d) and Fig. 11. It is now evident that during solidification, Ni acts as heterogeneous nuclei and the silver phase will grow along the preferred orientation of the already existing Ni in the composite. In a Ni-free composite, an even higher texture strength of the Ag phase was observed. The complete coherency of Ag and Ni in the presence of WC is one of the essential reasons behind the lowering of the Ag/Ni interfacial energy. It is also worth mentioning that Cu would also show such coherency. However it completely dissolves in the silver phase and fails to act as heterogeneous nuclei as

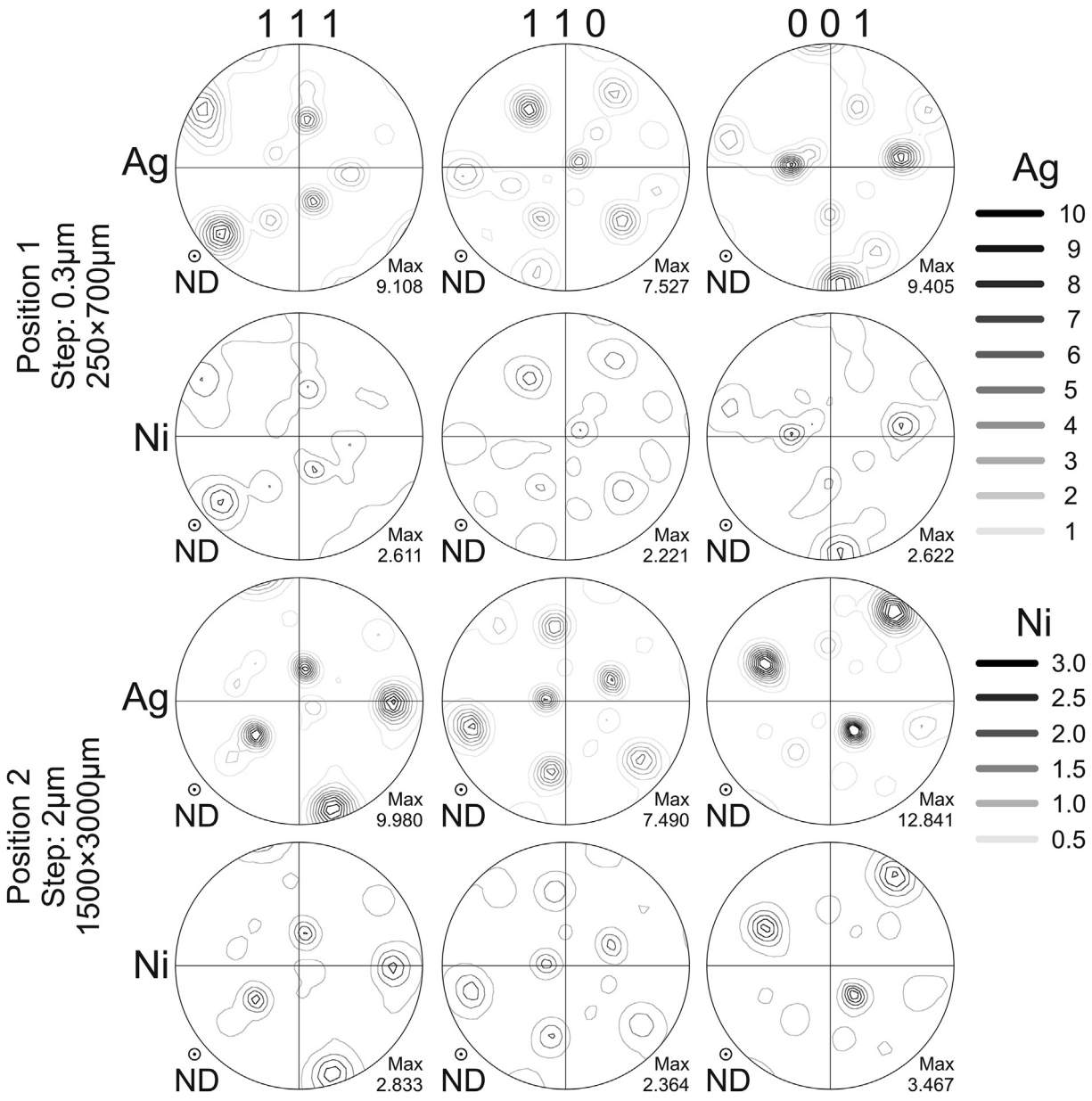

Fig. 11. (111), (110) and (001) pole figures of Ag and Ni phases in WC08Ni500 (Table 1) measured by electron backscattered diffraction. Normal direction, ND (⊥ to the plane of the paper) indicates the direction of powder pressing, silver infiltration and growth direction.

indicated by the large amount of undercooling (Fig. 5). Thus an element like Ni, which has an identical crystal structure and similar lattice parameters as silver but with limited solubility in Ag should also show similar effects.

Since the IPFs of the WC phase did not provide any information about the crystallographic preferred orientation, (0001), $(10\bar{1}0)$ and $(11\bar{2}0)$ pole figures were calculated for all the materials, as shown in Fig. 12. Although the texture strength of the WC phase in all the measurements is low, a weak but sharp texture can be observed which is consistent for all samples irrespective of the WC particle size and Ni content. Such monotonous and persistent texture would only correspond to a certain processing step which was common in all cases. According to the authors, such a preferred crystal rotation while exhibiting a weak texture can be attributed to the uniaxial pressing of the powders prior to sintering, where the WC particles lose their randomness and orient themselves along such a favored direction.

4. Conclusions

The wetting behavior of Ag on WC was investigated as a function of temperature and alloying elements like Ni and Cu. The contact angle measured from sessile drop experiments decreased with increasing temperature for the investigated pure silver and $AgNi_{0.15}$, $AgCu_{0.2}$, $AgCu_1$ and $AgCu_{0.2}Ni_{0.15}$ (all values in wt.%) alloys. Compared to Cu, Ni displayed a stronger influence in reducing the contact angle as a result of the adsorption of Ni at the Ag/WC interface, which was also supported by the preferential segregation of Ni at the Ag/WC interface during cooling in contrast to Cu.

Orientation imaging was mainly used to study the microstructure and texture of infiltrated Ag-WC-Ni (40 wt% WC and 0.07/5 wt % Ni) composites. Pushing of WC particles by the solidification front was observed for the materials containing finer WC particle size. The amount of Ni in the composite directly influenced the grain size of the Ag phase, since Ni grains act as heterogeneous nuclei.

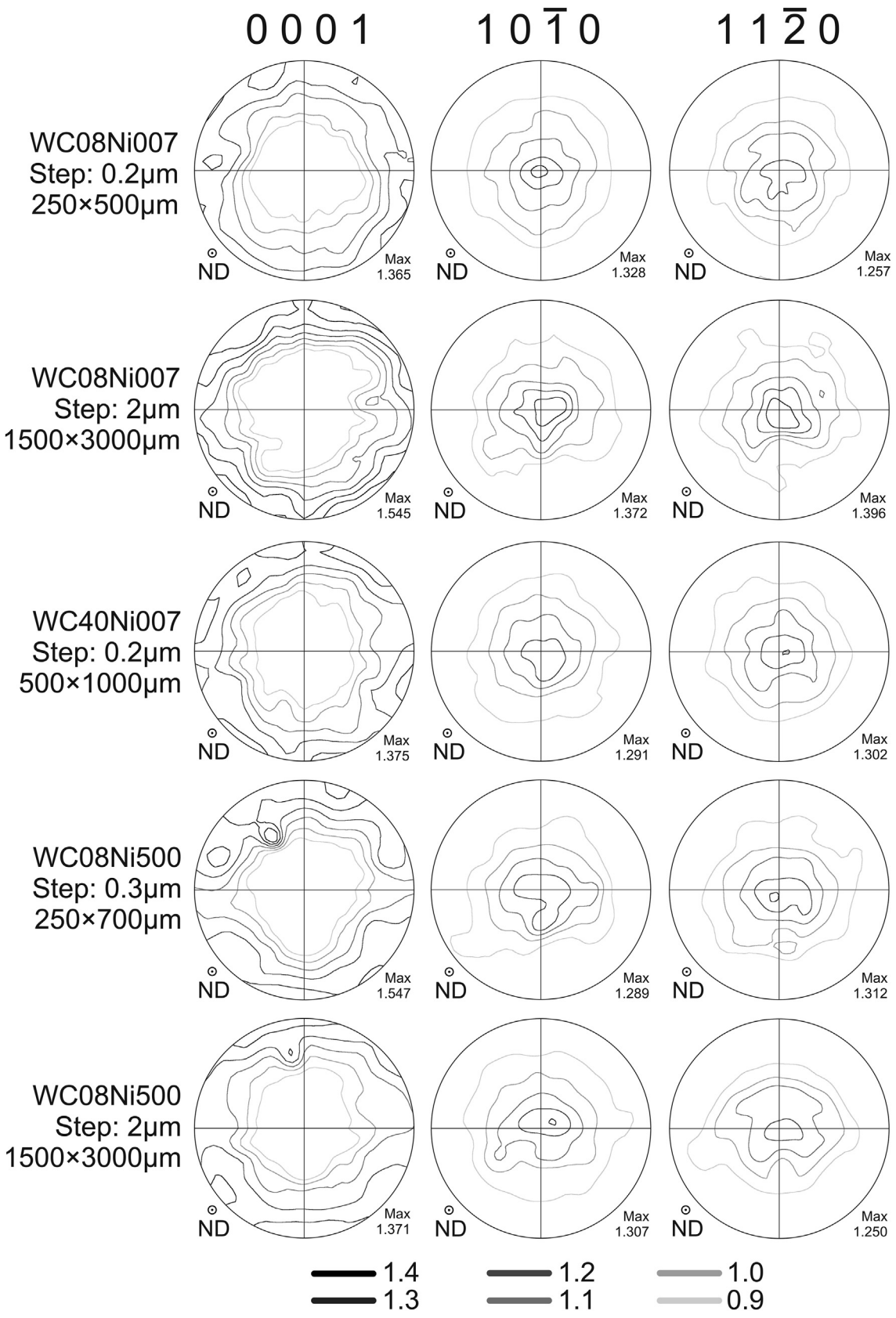

Fig. 12. (0001), (10$\bar{1}$0) and (11$\bar{2}$0) pole figures of the WC phase in Ag-WC-Ni materials as tabulated in Table 1, measured by electron backscattered diffraction. Normal direction, ND (⊥ to the plane of the paper) indicates the direction of powder pressing, silver infiltration and growth direction.

Complete coherency of the Ag and Ni phase was established post solidification. The texture of the WC phase was observed to be weak but sharp and was similar for all materials, most probably due to a preferential rotation of the WC grains during cold uniaxial pressing of the starting powder mixtures.

Acknowledgements

The authors gratefully acknowledge support from the Flemish government via the Hercules Foundation (project ZW09-09) for the electron probe micro-analyzer and the NanoSEM. The authors also greatly appreciate the help from Joris Van Dyck, KU Leuven for his assistance with the SVF17SP heating system and Frederik Vogeler, KU Leuven for his help with the surface roughness measurements.

References

[1] Application of contact materials, Umicore Technical Materials. http://technicalmaterials.umicore.com/CPM/en/Products/ContactMaterials/Applicationforcontactmaterials/(accessed April 24, 2016).
[2] C.-H. Leung, Arcing contact materials, silver refractory metals, in: Q.J. Wang, Y.-W. Chung (Eds.), Encyclopedia of Tribology, Springer, US, 2013, pp. 104–107, https://doi.org/10.1007/978-0-387-92897-5_404.
[3] N. Ray, B. Kempf, T. Mützel, L. Froyen, K. Vanmeensel, J. Vleugels, Effect of WC particle size and Ag volume fraction on electrical contact resistance and thermal conductivity of Ag–WC contact materials, Mater. Des. 85 (2015) 412–422, https://doi.org/10.1016/j.matdes.2015.07.006.
[4] M. Vijayakumar, A.M. Sriramamurthy, S.V. Nagender Naidu, Calculated phase diagrams of Cu-W, Ag-W and Au-W binary systems, Calphad 12 (1988) 177–184, https://doi.org/10.1016/0364-5916(88)90019-3.
[5] T. Sugita, S. Ebisawa, K. Kawasaki, Contact angles of gold and silver on a clean tungsten substrate, Surf. Sci. 20 (1970) 417–420, https://doi.org/10.1016/0039-6028(70)90192-5.
[6] N. Eustathopoulos, M.G. Nicholas, B. Drevet, Wettability at High Temperatures, Elsevier, 1999.
[7] T. Yamaguchi, K. Harano, K. Yajima, Spreading and reactions of molten metals on and with cemented carbides, in: J. Pask, A. Evans (Eds.), Surfaces and Interfaces in Ceramic and Ceramic-Metal Systems, Springer, US, 1981, pp. 503–511.
[8] N. Eustathopoulos, Wetting by liquid metals—application in materials processing: the contribution of the grenoble group, Metals 5 (2015) 350–370, https://doi.org/10.3390/met5010350.
[9] Hideo Nakae, Ryuichi Inui, Yosuke Hirata, Hiroyuki Saito, Effects of surface roughness on wettability, Acta Mater. 46 (1998) 2313–2318, https://doi.org/10.1016/S1359-6454(98)80012-8.
[10] F.Y.H. Lin, D. Li, A.W. Neumann, Effect of surface roughness on the dependence of contact angles on drop size, J. Colloid Interface Sci. 159 (1993) 86–95, https://doi.org/10.1006/jcis.1993.1300.
[11] K.T. Hong, H. Imadojemu, R.L. Webb, Effects of oxidation and surface roughness on contact angle, Exp. Therm. Fluid Sci. 8 (1994) 279–285, https://doi.org/10.1016/0894-1777(94)90058-2.
[12] A. Mortensen, I. Jin, Solidification processing of metal matrix composites, Int. Mater. Rev. 37 (1992) 101–128, https://doi.org/10.1179/imr.1992.37.1.101.
[13] P. Rohatgi, R. Asthana, The solidification of metal-matrix particulate composites, JOM 43 (1991) 35–41, https://doi.org/10.1007/BF03220566.
[14] A.F. Stalder, T. Melchior, M. Müller, D. Sage, T. Blu, M. Unser, Low-bond axisymmetric drop shape analysis for surface tension and contact angle measurements of sessile drops, Colloids Surfaces A Physicochem. Eng. Aspects 364 (2010) 72–81, https://doi.org/10.1016/j.colsurfa.2010.04.040.
[15] P. Protsenko, A. Terlain, N. Eustathopoulos, Wetting of W by liquid Pb and PbLi alloys and surface interactions, J. Nucl. Mater. 360 (2007) 265–271, https://doi.org/10.1016/j.jnucmat.2006.10.005.
[16] A.B.D. Cassie, Contact angles, Discuss. Faraday Soc. 3 (1948) 11–16, https://doi.org/10.1039/DF9480300011.
[17] H.R. de Macedo, A.G.P. da Silva, D.M.A. de Melo, The spreading of cobalt, nickel and iron on tungsten carbide and the first stage of hard metal sintering, Mater. Lett. 57 (2003) 3924–3932, https://doi.org/10.1016/S0167-577X(03)00242-8.
[18] X.J. Liu, F. Gao, C.P. Wang, K. Ishida, Thermodynamic assessments of the Ag-Ni binary and Ag-Cu-Ni ternary systems, J. Elec Materi 37 (2007) 210–217, https://doi.org/10.1007/s11664-007-0315-1.
[19] E. Lassner, W.-D. Schubert, Tungsten: Properties, Chemistry, Technology of the Elements, Alloys, and Chemical Compounds, Springer Science & Business Media, 1999.
[20] N.S. Hoyer, Process for Improving Homogeneity of Silver or Copper Refractory Contact Materials, 1957. US2813808 (A).
[21] R. Subramanian, J.H. Schneibel, Intermetallic bonded WC-based cermets by pressureless melt infiltration, Intermetallics 5 (1997) 401–408, https://doi.org/10.1016/S0966-9795(97)00010-1.
[22] J. Weidow, H.-O. Andrén, Binder phase grain size in WC–Co-based cemented carbides, Scr. Mater. 63 (2010) 1165–1168, https://doi.org/10.1016/j.scriptamat.2010.08.025.
[23] K.P. Mingard, B. Roebuck, J. Marshall, G. Sweetman, Some aspects of the structure of cobalt and nickel binder phases in hardmetals, Acta Mater. 59 (2011) 2277–2290, https://doi.org/10.1016/j.actamat.2010.12.004.
[24] N. Ray, B. Kempf, G. Wiehl, T. Mützel, F. Heringhaus, L. Froyen, K. Vanmeensel, J. Vleugels, Novel processing of Ag-WC electrical contact materials using spark plasma sintering, Mater. Des. 121 (2017) 262–271, https://doi.org/10.1016/j.matdes.2017.02.070.
[25] R. Sasikumar, T.R. Ramamohan, B.C. Pai, Critical velocities for particle pushing by moving solidification fronts, Acta Metall. 37 (1989) 2085–2091, https://doi.org/10.1016/0001-6160(89)90094-1.
[26] A.W. Neumann, J. Szekely, E.J. Rabenda, Thermodynamics of particle engulfment by solidifying melts, J. Colloid Interface Sci. 43 (1973) 727–732, https://doi.org/10.1016/0021-9797(73)90417-7.
[27] S.N. Omenyi, A.W. Neumann, Thermodynamic aspects of particle engulfment by solidifying melts, J. Appl. Phys. 47 (1976) 3956–3962, https://doi.org/10.1063/1.323217.
[28] G.F. Bolling, J. Cissé, A theory for the interaction of particles with a solidifying front, J. Cryst. Growth 10 (1971) 56–66, https://doi.org/10.1016/0022-0248(71)90046-7.
[29] A.A. Chernov, A.M. Mel'nikova, Soviet Phys. Crystallogr. 10 (1966) 672–675.
[30] A.M. Zubko, V.G. Lobanov, V.V. Nikonova, Soviet Phys. Crystallogr. 18 (1973) 239–241.
[31] M.K. Surappa, P.K. Rohatgi, Heat diffusivity criterion for the entrapment of particles by a moving solid-liquid interface, J. Mater Sci. 16 (1981) 562–564, https://doi.org/10.1007/BF00738658.
[32] B. Giordanengo, N. Benazzi, J. Vinckel, J.G. Gasser, L. Roubi, Thermal conductivity of liquid metals and metallic alloys, J. Non-Crystalline Solids 250–252 (1999) 377–383, https://doi.org/10.1016/S0022-3093(99)00268-9. Part 1.
[33] W. Neumann, Thermal Diffusivity of Cemented Carbides, in: T. Ashworth, D.R. Smith (Eds.), Thermal Conductivity 18, first ed., Springer, US, Boston, MA, 1985, pp. 473–481.
[34] J. Cissé, G.F. Bolling, A study of the trapping and rejection of insoluble particles during the freezing of water, J. Cryst. Growth 10 (1971) 67–76, https://doi.org/10.1016/0022-0248(71)90047-9.
[35] J. Cissé, G.F. Bolling, The steady-state rejection of insoluble particles by salol grown from the melt, J. Cryst. Growth 11 (1971) 25–28, https://doi.org/10.1016/0022-0248(71)90158-8.
[36] N. Ray, B. Kempf, T. Mützel, F. Heringhaus, L. Froyen, K. Vanmeensel, J. Vleugels, Effect of Ni addition on the contact resistance of Ag-WC electrical contacts, J. Alloys Compd. 670 (2016) 188–197, https://doi.org/10.1016/j.jallcom.2016.02.037.